



Cite this: DOI: 10.1039/c4dt02717e

# The role of reaction conditions in the polymorphic control of $\text{Eu}^{3+}$ doped $\text{YInO}_3$ : structure and size sensitive luminescence†

R. Shukla,<sup>a</sup> Santosh K. Gupta,<sup>b</sup> V. Grover,<sup>\*a</sup> V. Natarajan<sup>b</sup> and A. K. Tyagi<sup>\*a</sup>

With the aim of exploring the effect of particle size and different polymorphic structures on the luminescence behaviour of  $\text{Eu}^{3+}$  ions, all in a single compound, the  $\text{YInO}_3:\text{Eu}^{3+}$  system was synthesized. Metastable C-type modification could be obtained in  $\text{YInO}_3$  nanopowders synthesized by gel combustion. The broadening in Raman modes has been related to both the particle size and the strain in the metastable C-type modification. The hexagonal polymorph of  $\text{YInO}_3$ , with a layered structure, quite unlike the C-type modification, could be obtained by heating nanopowders to 1175 °C. Such a change in the structure, leading to different site symmetries for  $\text{Eu}^{3+}$  ions exhibited a tremendous bearing on its luminescence behaviour. Detailed steady state and time resolved luminescence studies revealed a highly distorted local site symmetry for the  $\text{Y}^{3+}$  ion in hexagonal  $\text{YInO}_3$ . The nano C-type  $\text{YInO}_3$  exhibited greater asymmetry and a shorter lifetime as compared to the bulk C-type  $\text{YInO}_3$ , attributable to more surface defects in the case of the former. The Judd–Ofelt parameters ( $\Omega_2$  and  $\Omega_4$ ) were determined which established a much higher asymmetry in the hexagonal modification. Along with higher lifetime, the hexagonal polymorph also possessed superior quantum yield values. In addition to providing a significant insight into the structure–luminescence correlation in this study, we propose an efficient red phosphor with a high red color purity.

Received 5th September 2014,  
Accepted 5th December 2014

DOI: 10.1039/c4dt02717e

www.rsc.org/dalton

## 1. Introduction

It is a widely known fact that the control of the polymorph for a particular compound under desired conditions is very vital for designing materials with favourable properties.<sup>1,2</sup> Many a times, the existence of a desired property in a compound can be attributed to its structure, symmetry and more importantly to the local arrangements of atoms or ions in the compound. It has been observed that a compound in a particular structure or in the polymorphic state possesses important functional properties while the other polymorphic modifications of the same compound might not exhibit these properties. In light of this, it becomes essential to investigate the local structure to generate a greater understanding of the structural control of properties. Of late, the luminescence behaviour of lanthanide ions, in particular,  $\text{Eu}^{3+}$ , is being extensively employed as a structural probe.<sup>3</sup> The reason behind this is that some transitions in  $\text{Eu}^{3+}$  are extremely sensitive to local symmetry which

makes the  $\text{Eu}^{3+}$  ions the favoured luminescent structural probe.

$\text{YInO}_3$  belongs to the hexagonal  $\text{ABO}_3$  class of compounds which despite possessing a similar nominal formula do not crystallize in the perovskite structure. The  $\text{ABO}_3$  composition crystallizes in the hexagonal structure when the tolerance factor given by  $(r_A + r_O)/\sqrt{2}(r_B + r_O)$  is less than that required for orthorhombic perovskites.<sup>4</sup> A hexagonal  $\text{ABO}_3$  possesses layered structures composed of  $\text{AO}_7$  polyhedra and  $\text{BO}_5$  trigonal bipyramids.<sup>5</sup> It has been reported that  $\text{YInO}_3$  transforms into C-type rare earth oxide structures at higher temperatures.<sup>6</sup> They have been investigated for diverse applications like color pigments<sup>7</sup> and as photocatalysts.<sup>8</sup> These materials have assumed a lot of importance recently because of the possibility of existence of geometric ferroelectricity.<sup>9</sup> These are called improper ferroelectrics and their electrical behavior has been attributed to the non-centrosymmetric atomic arrangement of the crystal.<sup>9</sup> Since these compounds do not owe their ferroelectric properties to  $d^0$  ions, as in conventional ferroelectrics, they offer new templates for designing magnetic-ferroelectrics that have been historically difficult to achieve, but are appealing for 'spintronics' applications.<sup>10</sup> In our previous work on rare earth indates, we have demonstrated how the local structure at A- and B-sites is instrumental in controlling the

<sup>a</sup>Chemistry Division, Bhabha Atomic Research Centre, Mumbai-400085, India<sup>b</sup>Radiochemistry Division, Bhabha Atomic Research Centre, Mumbai-400085, India.

E-mail: vinita@barc.gov.in, aktyagi@barc.gov.in

†Electronic supplementary information (ESI) available. See DOI: 10.1039/c4dt02717e

electrical behavior of this class of compounds. The importance of the local environment around A- and B-cations and their expression in the bulk electrical behavior in perovskites and other complex oxides has been a front area of research.<sup>11</sup> Herein, due to the properties being controlled primarily by the structure adopted by the  $ABO_3$  compositions, this class forms an interesting case study for probing the local structure using various techniques.

In view of the emphasis laid on the fine structural features and the electrical properties exhibited by the hexagonal indates, this study aimed at synthesizing  $YInO_3:Eu$  in two different polymorphic modifications and exploring the local structure and its influence on  $Eu^{3+}$  luminescence. This may pave the way for obtaining materials with a superior luminescence behavior as well by suitable polymorphic control.

## 2. Experimental

AR (Analytical Reagent) grade powders of  $Y_2O_3$ ,  $In_2O_3$ ,  $Eu_2O_3$  and glycine were used as the starting reagents. The synthesis of  $YInO_3:1 \text{ mol } Eu^{3+}$  ( $Y_{0.99}Eu_{0.01}InO_3$ ) was carried out by the self-propagating gel combustion method. Stoichiometric amounts of  $Y_2O_3$  (894.22 mg),  $Eu_2O_3$  (1.11 mg) and  $In_2O_3$  (1110.54 mg) were dissolved in a minimum amount of nitric acid and the combustion was carried out in the presence of glycine as the fuel. The combustion reaction was performed in the fuel-deficient stoichiometry wherein the oxidant-to-fuel (O/F) ratio was kept at 1 : 1.5 (the stoichiometric O/F ratio for this reaction is 1 : 3.33). Thus, the amount of glycine taken for this combustion was 900 mg. No further pH adjustments were made. The solution was dehydrated to highly viscous liquids (gels). At this stage, the temperature was raised to 250 °C which led to swelling followed by the auto-ignition of the viscous liquid, with a rapid evolution of a large volume of gases to produce voluminous powders. The powders were calcined at 600 °C and partitioned into three parts. Two of these were then heated at 900 °C and 1175 °C in static air for 8 h each in order to obtain different polymorphs.

X-Ray diffraction (XRD) studies were performed using a monochromatized  $Cu K\alpha$  radiation on a PANalytical Xpert Pro. Silicon was used as an external standard. The patterns were refined using Rietveld refinement and lattice parameters were determined. Raman spectroscopic measurements on pelletized samples were performed on a micro/macro-Raman spectrometer (make-LABRAM-1, France) using a 488 nm line of an  $Ar^{+}$  ion laser for excitation. A single monochromator spectrometer equipped with a Peltier-cooled CCD detector in the backscattering geometry was used for collecting the scattered Raman signal. The laser line was focused on a flat surface of the sample using an optical microscope (Olympus BX-40, 50× objective lens) connected to the spectrometer. The spectra recorded were averaged out of 50 scans with a time interval of 2 s and a resolution of  $2 \text{ cm}^{-1}$ .

PL data were recorded on an Edinburgh CD-920 unit equipped with M 300 monochromators. The data acquisition

and analysis were done using F-900 software provided by Edinburgh Analytical Instruments, UK. A xenon flash lamp with a frequency range of 10–100 Hz was used as the excitation source. First the excitation spectrum was recorded by fixing  $\lambda_{em}$  at 610 nm ( ${}^5D_0 \rightarrow {}^7F_2$  of  $Eu(III)$ ). The  $\lambda_{ex}$  was selected so as to obtain the maximum fluorescence output. All the emission spectra were recorded in the wavelength range of 350–750 nm with a step of 0.5 nm. The emission spectrum for a particular sample was recorded with a lamp frequency of 100 Hz. Multiple scans (at least five) were taken to minimize the fluctuations in the peak intensity and maximize the S/N ratio. Fluorescence lifetime measurements are based on the well established time-correlated single-photon counting (TCSPC) technique. Lifetime studies were done in a time range of 10 ms where the frequency of the Xe lamp was fixed at 10 Hz.  $\lambda_{ex}$  and  $\lambda_{em}$  were kept at 256 and 610 nm, respectively. All the life-time data obtained were fitted with a single exponential decay by an equation of the type,  $I(t) = A_{exp}(-t/\tau)$ , where  $t$  is the lifetime of the  ${}^5D_0$  excited state.

## 3. Results and discussion

### 3.1 X-ray diffraction studies

$YInO_3:Eu$  was synthesized by a self-assisted gel combustion route followed by calcination at 600 °C. The XRD pattern of the calcined powder (Fig. 1(a)) reveal the C-type structure (space group:  $Ia\bar{3}$ ) for this compound. The X-ray peaks are relatively broad indicating the nano-nature of the powder. The nanopowder was heated at 900 °C and its XRD pattern is depicted in Fig. 1(b). It is obvious that the C-type modification is retained at 900 °C as well. Both the XRD patterns are qualitatively similar except for the narrowing down of the X-ray peaks indicating an increase in the particle size on heating the sample at higher temperatures. Interestingly, the XRD pattern for the sample heated at 1175 °C (Fig. 1(c)) is completely different from that observed at 600 °C and 900 °C and pertains to the hexagonal modification of  $YInO_3$  (space group:  $P6_3cm$ ).

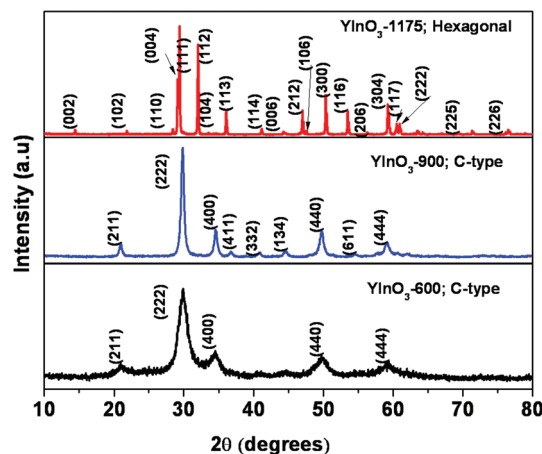


Fig. 1 X-ray diffraction patterns for  $YInO_3$  heated at (a) 600 °C, (b) 900 °C and (c) 1175 °C.

This implies that the temperature increment is accompanied by a polymorphic phase transition.

The X-ray diffraction patterns for  $\text{YInO}_3$  annealed at 900 °C and 1175 °C were refined using Rietveld refinement.<sup>12</sup> It must be noted that the samples of  $\text{YInO}_3$ : 1 mol%  $\text{Eu}^{3+}$  heated at 600 °C, 900 °C and 1175 °C will be referred to as  $\text{YInO}_3$ -600,  $\text{YInO}_3$ -900 &  $\text{YInO}_3$ -1175 respectively. The Rietveld-fitted XRD patterns for  $\text{YInO}_3$ -900 and  $\text{YInO}_3$ -1175 are shown in Fig. S-1 (ESI-I†). Table S-1 (ESI-II†) contains the refined parameters for  $\text{YInO}_3$ -900 and  $\text{YInO}_3$ -1175. The C-type (Sp. Group  $Ia\bar{3}$ ) or the bixbyite structure adopted by  $\text{YInO}_3$ -600 and  $\text{YInO}_3$ -900 is an ordered structure based on the F-type fluorite lattice. It is obtained by the removal of a quarter of anions and the subsequent rearrangements of cations.<sup>4</sup> The cations possess six-fold irregular polyhedra in the C-type structure as compared to the 8-fold regular polyhedra in a fluorite-type structure.<sup>13</sup> On the other hand the hexagonal structure (sp. Group:  $P6_3cm$ ) has no crystallographic relationship to the C-type and is a layered structure wherein the layers of  $\text{BO}_5$  trigonal bipyramids are joined by the  $\text{YO}_7$  polyhedra.<sup>5</sup> The appearance of the hexagonal phase at higher temperatures and C-type at lower temperatures is also a significant observation. As has been reported,<sup>14</sup> the tolerance factor (which predicts the structure adopted by the  $\text{ABO}_3$  compositions) for  $\text{YInO}_3$  is higher than that corresponding to the bixbyite structure and accordingly it should crystallize in the hexagonal structure at room temperature. The stabilization of the metastable C-type phase for  $\text{YInO}_3$  can be attributed to the kinetic stability brought about by the non-equilibrium synthesis method adopted here which brings about the randomization of Y and In ions, despite the ionic size difference, favoring the C-type configuration. These structural details have been discussed in detail in our previous studies on similar systems.<sup>14,15</sup>

### 3.2 Vibrational spectroscopic studies on the polymorphs

Raman spectroscopy is an invaluable technique to study the structural variations at the microstructural level. Raman spectroscopic studies were performed on all three samples *i.e.*  $\text{YInO}_3$ -600,  $\text{YInO}_3$ -900 and  $\text{YInO}_3$ -1175 and the Raman spectra are depicted in Fig. 2. The Raman spectra of  $\text{YInO}_3$ -600 and  $\text{YInO}_3$ -900 show the typical modes observed for the C-type rare earth oxides. The Raman modes predicted for an ideal C-type structure are  $4A_g + 4E_g + 14F_g$ , where  $A_g$  is the Raman active symmetric stretching vibration,  $F_g$  is the Raman active triply degenerate symmetric stretching vibration, and  $E_g$  is the Raman active symmetric doubly degenerate bending vibration. The most intense band occurs at around  $380\text{ cm}^{-1}$  (Fig. 2(a and b)), which can be attributed to the ( $F_g + A_g$ ) mode of the (Y,In) $\text{O}_6$  octahedra.<sup>16</sup> The highest band at  $612\text{ cm}^{-1}$  may be assigned to the (Y,In)–O stretch. It is obvious from the Raman spectra that  $\text{YInO}_3$ -600 and  $\text{YInO}_3$ -900 possess a similar kind of structure even at the microscopic level. However, it is noticeable that certain C-type features at 300, 483 *etc.* which were not visible at 600 °C have started to become visible at 900 °C and this can be attributed to an increased crystallinity achieved after annealing at 900 °C.

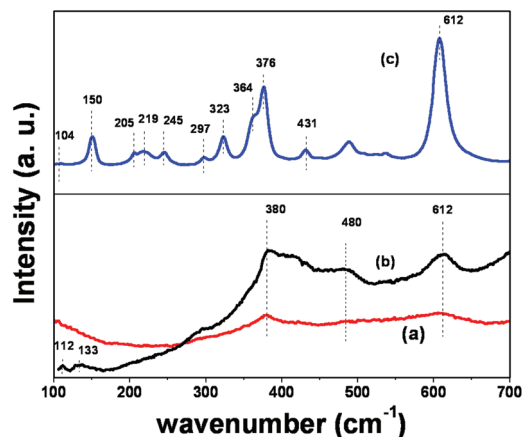


Fig. 2 Raman spectra of (a)  $\text{YInO}_3$ -600, (b)  $\text{YInO}_3$ -900 and (c)  $\text{YInO}_3$ -1175.

It must be mentioned that the Raman modes observed for  $\text{YInO}_3$ -600 and  $\text{YInO}_3$ -900 are tremendously broadened. The immense broadening in Raman modes has generally been attributed to the smaller particle size<sup>17</sup> and hence this explains the broadening observed for  $\text{YInO}_3$ -600. Even though the particle size increases on annealing the sample at 900 °C, the broadening in the Raman modes does not decrease significantly. This may be explained on the basis of the prevalence of cation heterogeneity in the lattice. The cation heterogeneity leads to a spread in the vibration frequency of a particular mode which manifests as its broadening. On heating the sample to a higher temperature, *i.e.* 1175 °C, it transforms to the stable hexagonal phase thus showing a completely different Raman spectrum with much narrower Raman modes. The Raman spectrum of hexagonal  $\text{YInO}_3$  has been discussed in our previous work.<sup>14</sup> It must be noted that to the best of our knowledge there has been no detailed Raman analysis of  $\text{YInO}_3$  in the literature and the analysis of the Raman spectrum of hexagonal  $\text{YInO}_3$  (both in the present work and in ref. 14) has been based on the Raman spectrum exhibited by  $\text{YMnO}_3$  which crystallizes in the same space group as  $\text{YInO}_3$  and has been investigated by dedicated Raman studies.<sup>18</sup> It is also noticeable that the same composition of  $\text{YInO}_3$ , when adopts the thermodynamically stable modification (which is hexagonal in this case), shows narrower Raman bands which proves the decrease in the strain prevalent in the lattice. Also, since in a hexagonal modification both Y and In occupy distinct sites, there is no cation heterogeneity at any site which again is manifested in the narrower bands. The increase in the particle size upon annealing at higher temperatures also contributes to the narrowing down of the Raman modes.

### 3.3 Photoluminescence (excitation & emission spectroscopy)

In order to study the local site symmetry of  $\text{Y}^{3+}$  in all the three samples, and its effect on the luminescence behavior of symmetry-sensitive  $\text{Eu}^{3+}$  ions, detailed photoluminescence studies were performed. The excitation spectrum of  $\text{YInO}_3$ -600 nanoparticles monitored at an emission wavelength of 610 nm is

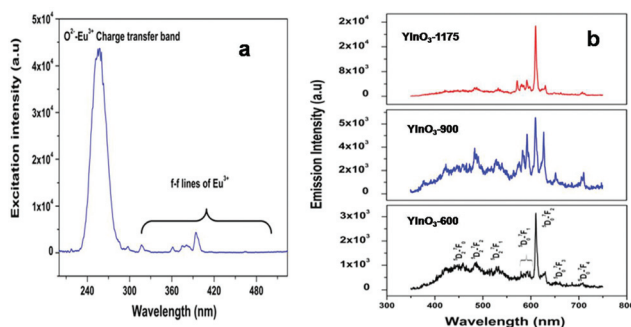


Fig. 3 (a) Excitation spectrum of  $\text{YInO}_3:\text{Eu}^{3+}$  ( $\lambda_{\text{em}} = 610 \text{ nm}$ ). (b) Emission intensity of  $\text{YInO}_3:\text{Eu}^{3+}$  as a function of annealing temperature ( $\lambda_{\text{ex}} = 256 \text{ nm}$ ).

shown in Fig. 3(a). It consists of a strong broad band in the range of 220–280 nm and very weak lines in the region of 300–550 nm. A broad hump observed in the region of 220–280 nm peaking at 256 nm can be attributed to the  $\text{O}^{2-} \rightarrow \text{Eu}^{3+}$  charge transfer band (CTB) and the weaker lines in the higher wavelength regions (350–550 nm) are assigned to the interconfigurational f-f transitions of the  $\text{Eu}^{3+}$  ions. Fig. 3(b) depicts the emission spectra of the samples annealed at 600 °C, 900 °C and 1175 °C at 256 nm excitation.

A glance at Fig. 3 reveals that the broad spectral features of the  $\text{Eu}^{3+}$  activator remain the same for all the samples. The spectra exclusively contain very weak lines of  ${}^5\text{D}_2 \rightarrow {}^7\text{F}_0$  (465 nm),  ${}^5\text{D}_2 \rightarrow {}^7\text{F}_2$  (490 nm) and  ${}^5\text{D}_1 \rightarrow {}^7\text{F}_1$  (535 nm),<sup>19</sup> superposed over a broad host emission, and the strong lines of  ${}^5\text{D}_0 \rightarrow {}^7\text{F}_1$  (594 nm),  ${}^5\text{D}_0 \rightarrow {}^7\text{F}_2$  (614 nm),  ${}^5\text{D}_0 \rightarrow {}^7\text{F}_3$  (653 nm) and  ${}^5\text{D}_0 \rightarrow {}^7\text{F}_4$  (704 nm). In all the samples, the broad emission can be assigned to the presence of oxygen related defects in  $\text{YInO}_3$ .<sup>20</sup> Upon excitation at 393 nm, corresponding to the  ${}^7\text{F}_0 \rightarrow {}^5\text{L}_6$  band of  $\text{Eu}^{3+}$ , emission properties similar to that of CTB excitation were observed. It is also noticed that the intensities of the emission bands are relatively lower, when excited with the characteristic absorption band of  $\text{Eu}^{3+}$  ions at 393 nm, compared to that of the emission intensities obtained with the LMCT (ligand to metal charge transfer) excitation band (256 nm). This may be due to the fact that the  $\text{Eu}^{3+}$  absorption bands corresponding to the f-f transitions are forbidden and exhibit poor absorptivities in the UV region and hence a relatively weaker emission is exhibited. It should be noticed that the emission spectra of the  $\text{YInO}_3:\text{Eu}^{3+}$  phosphors consist of emissions from the higher energy levels ( ${}^5\text{D}_1$  and  ${}^5\text{D}_2$ ) as well. This is interesting because it has been reported that the  ${}^5\text{D}_{1,2,3} \rightarrow {}^7\text{F}_j$  lines usually appear in the emission spectra of compounds with a low-lattice phonon energy. Thus, the presence of emission lines from higher excited states of  $\text{Eu}^{3+}$  implies the low phonon vibration energy for the host  $\text{YInO}_3$  lattice. This could be significant in the context of the development of new host lattices with a high fluorescence yield. Further, the Stark splitting in the emission spectra is a proof of superior crystallinity of the samples.

The decay curves corresponding to the  ${}^5\text{D}_0$  level of  $\text{Eu}^{3+}$  ions in all the three  $\text{YInO}_3$  samples annealed at different tem-

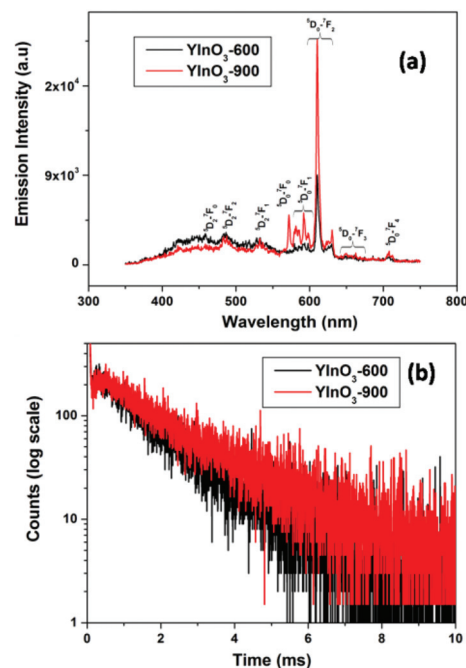


Fig. 4 (a) Room temperature emission spectra from the bulk and nanoparticles of 1.0 mol%  $\text{Eu}^{3+}$  doped  $\text{YInO}_3$  ( $\text{YInO}_3$ -900 and  $\text{YInO}_3$ -600). The samples were excited at 256 nm. (b) Decay curve corresponding to the  ${}^5\text{D}_0$  level of  $\text{Eu}^{3+}$  in a bulk and nanoparticles of 1.0 mol%  $\text{Eu}^{3+}$  doped  $\text{YInO}_3$ . The samples were excited at 256 nm and the emissions were monitored at 610 nm.

peratures were also obtained to gain an in-depth understanding and are depicted in Fig. 4(b) and 6(b). All the decay profiles could be fitted using the monoexponential decay:

$$I = I_0 \exp(-t/\tau)$$

where  $t$  is the times of measurement and  $\tau$  are the decay time values or the lifetime values. The lifetime values were obtained to be 1.47, 1.62 and 1.96 ms respectively for the  $\text{YInO}_3$ -600,  $\text{YInO}_3$ -900 and  $\text{YInO}_3$ -1175. Single lifetime values indicate a similar and homogeneous environment for  $\text{Eu}^{3+}$  in  $\text{YInO}_3$ .

### 3.4 Effect of size and polymorphic modification on luminescence behaviour

The optical characterisation of the  $\text{YInO}_3:\text{Eu}$  system was considered worth exploring because it provides a single system, wherein using a sensitive luminescence probe like  $\text{Eu}^{3+}$ , the effect of size ( $\text{YInO}_3$ -600 and  $\text{YInO}_3$ -900) and two different polymorphs ( $\text{YInO}_3$ -900 and  $\text{YInO}_3$ -1175) on the local structural distortions and luminescence can be investigated.

**3.4.1 Effect of size.** Fig. 4(a) and (b) show a comparison of emission spectra and luminescence decay profiles for  $\text{YInO}_3$ -600 and  $\text{YInO}_3$ -900. It is well known that photo-luminescence due to the  ${}^5\text{D}_0 \rightarrow {}^7\text{F}_1$  transition of  $\text{Eu}^{3+}$  is a magnetic dipole transition while  ${}^5\text{D}_0 \rightarrow {}^7\text{F}_2$  is an electric dipole allowed transition. The latter transition is allowed only for sites with no inversion center and it is very sensitive to the local environment around  $\text{Eu}^{3+}$  ions. Thus, the intensity ratio of these

transitions serves as a very effective spectroscopic parameter for monitoring the symmetry of the site occupied by  $\text{Eu}^{3+}$ .

This ratio, also known as the asymmetric ratio of luminescence ( $I$ ) (defined as  $I = I_{(5D_0-7F_2)}/I_{(5D_0-7F_1)}$ ) is calculated from the emission spectra and the higher is this ratio, the lower is the site symmetry. The values of “ $I$ ” are found to be 1.89 and 1.26 for  $\text{YInO}_3\text{-600}$  and  $\text{YInO}_3\text{-900}$  respectively. The significantly higher value of  $I$  for  $\text{YInO}_3\text{-600}$  suggests that the  $\text{Eu}^{3+}$  ions are occupying a more distorted environment in the nanoparticles compared to the bulk. This can be explained on the basis of a higher surface to volume ratio in the nanopowders which leads to a significantly higher fraction of  $\text{Eu}^{3+}$  ions on the surface which are obviously exposed to a more asymmetric environment and hence the higher value of  $I$ . In addition to the asymmetric ratio, the luminescence lifetime corresponding to the excited state of the  $\text{Eu}^{3+}$  ions and their decay profiles are also very sensitive to the changes in the environment. The lower emission intensity and luminescence lifetime for  $\text{YInO}_3\text{-600}$  (1.47 ms) as compared to  $\text{YInO}_3\text{-900}$  (1.62 ms) again indicate the presence of a large number of surface defects in the former which provides additional pathways for the non-radiative decay channels. This is further supported by the lower quantum efficiency (Table 1) of  $\text{YInO}_3\text{-600}$  as compared to  $\text{YInO}_3\text{-900}$  indicating that non-radiative decay dominates the relaxation processes in  $\text{YInO}_3\text{-600}$ .

As it was discussed earlier, both  $\text{YInO}_3\text{-600}$  and  $\text{YInO}_3\text{-900}$  crystallize in the C-type structure. It is pertinent to mention here that in the C-type structure ( $\text{A}_2\text{O}_3$ ), the A-cation enters into crystallographically non-equivalent sites of six-fold coordination.<sup>13</sup> One of these sites has the cation on a distorted cubic lattice with oxygen vacancies on the face diagonal with the point symmetry of  $C_2$ . The other site, with  $S_6$  symmetry, possesses the inversion symmetry and has oxygen vacancies lying on the body diagonal of the cube. The schematics of  $S_6$  and  $C_2$  sites are shown in Fig. 5.

Considering the fact that the ED transitions (such as  $^5D_0 \rightarrow ^7F_2$  red emission at about 610 nm) originate from sites with no inversion symmetry, they can be safely assigned to be emitted by ions occupying the  $C_2$  site. The orange emission at 592 nm belongs to the MD  $^5D_0 \rightarrow ^7F_1$  transitions of  $\text{Eu}^{3+}$ , and this transition hardly varies with the crystal field strength and is thus assigned to both  $C_2$  and  $S_6$  sites. An increase in the temperature will lead to increased randomisation in the

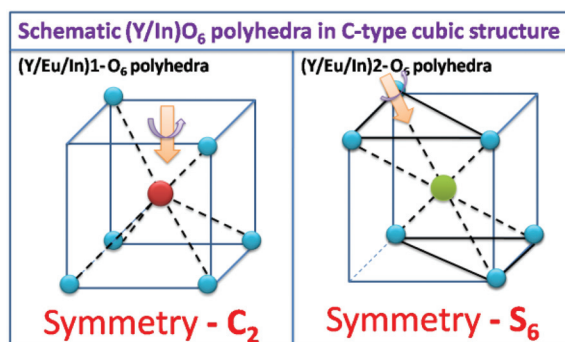


Fig. 5 Schematics of two types of sites ( $S_6$  and  $C_2$ ) occupied by the trivalent cation in the C-type structure.

cationic distribution over both the sites and this will also cause a decrease in the asymmetry ratio. In fact, a careful observation of Fig. 4(a) will emphasize this. However, the effect of this factor on the value of the asymmetry ratio will be similar to that which brought about an increase in the particle size (decreased surface defects) as discussed earlier and hence its contribution to the decrease in the asymmetry ratio cannot be delineated.

**3.4.2 Effect of polymorphic transition.** Fig. 6(a) and (b) show the emission spectra and luminescence decay profiles for  $\text{YInO}_3\text{-900}$  and  $\text{YInO}_3\text{-1175}$ . Further annealing the sample

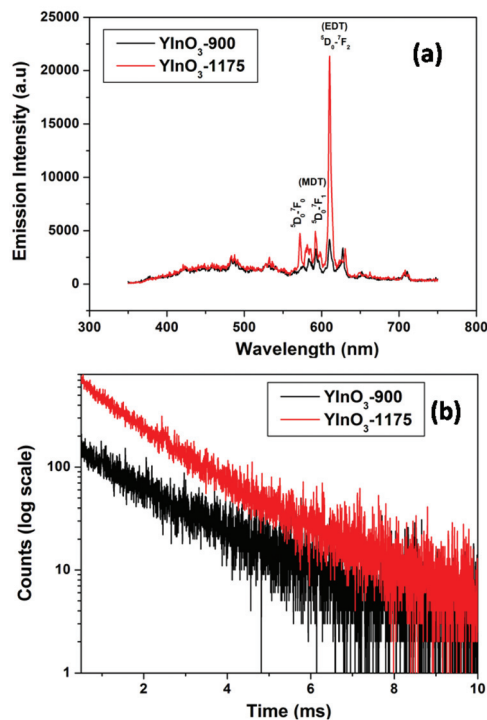


Fig. 6 (a) Room temperature emission spectra of  $\text{YInO}_3\text{-900}$  and  $\text{YInO}_3\text{-1175}$ . The samples were excited at 256 nm. (b) Decay curves corresponding to the  $^5D_0$  level of  $\text{Eu}^{3+}$  for  $\text{YInO}_3\text{-900}$  and  $\text{YInO}_3\text{-1175}$ . The samples were excited at 256 nm and the emissions were monitored at 610 nm.

**Table 1** Radiative and non-radiative decay rates, quantum efficiencies ( $^5D_0$  level), intensity ratios between the  $^5D_0 \rightarrow ^7F_2$  and  $^5D_0 \rightarrow ^7F_1$  transitions and Judd–Ofelt intensity parameters of the  $\text{Eu}^{3+}$  doped  $\text{YInO}_3$ . ( $\Omega_2$  and  $\Omega_4$ : Judd–Ofelt parameters;  $A_{NR}$  and  $A_R$ : non-radiative and radiative transition probability respectively;  $\eta$ : quantum efficiency;  $I_{02}/I_{01}$ : asymmetry ratio)

$\text{Eu}^{3+}$ doped	$\Omega_2$ ( $10^{-20}$ cm $^2$ )	$\Omega_4$ ( $10^{-20}$ cm $^2$ )	$\Omega_2/\Omega_4$	$A_{NR}$ ( $s^{-1}$ )	$A_R$ ( $s^{-1}$ )	$\eta$ (%)	$I_{02}/I_{01}$
$\text{YInO}_3\text{-600}$	2.96	3.29	0.89	987	448	31	1.89
$\text{YInO}_3\text{-900}$	2.04	3.04	0.67	786	412	34	1.26
$\text{YInO}_3\text{-1175}$	2.95	2.32	1.27	652	369	36	1.96

at 1175 °C changes the phase and this gives an opportunity to study the effect of phase change on the luminescence behaviour in the same compound.

Here again, the emission spectrum of YInO<sub>3</sub>-1175 exhibits the electric dipole transition to be much more prominent than the magnetic-dipole transition and the asymmetry ratio (*I*) for Eu<sup>3+</sup> is calculated to be 1.96. A significantly higher value of *I* for YInO<sub>3</sub>-1175 as compared to YInO<sub>3</sub>-600 suggests that the Eu<sup>3+</sup> ions are in a much more asymmetric environment. An extremely low site symmetry around Eu<sup>3+</sup> in hexagonal YInO<sub>3</sub> is also supported by the appearance of a relatively intense <sup>5</sup>D<sub>0</sub>→<sup>7</sup>F<sub>0</sub> line (~575 nm) transition. It is known that radiative transitions from <sup>5</sup>D<sub>0</sub> to levels with *J* = 0 or odd *J* (*J* = 3, 5) are both ED and MD forbidden, and that is why only weak transitions from <sup>5</sup>D<sub>0</sub> to these levels are observed due to the CF induced *J*-mixing effect and this is in fact allowed for very few site symmetries.<sup>21</sup> Indeed a closer look at the structure of hexagonal rare earth indates<sup>5</sup> reveals a trigonal anti-prismatic coordination for Y<sup>3+</sup> (and consequently Eu<sup>3+</sup>) ions which is very asymmetric. These results were further validated by life time measurement studies shown in Fig. 4. The lifetime value for YInO<sub>3</sub>-1175 is 1.96 ms which is much higher than for YInO<sub>3</sub>-900. This is because of the asymmetric environment of Eu<sup>3+</sup> in YInO<sub>3</sub>-1175 compared to YInO<sub>3</sub>-900; as a result selection rules get relaxed comparatively enhancing the lifetime for the f-f transition. Also because of the high temperature annealing of the system, agglomeration or clustering of the particles take place thereby reducing the surface to volume ratio. This in turn reduces the number of inherent defect centers which are sources for non-radiative pathways thus increasing the PL intensity and the decay time of Eu<sup>3+</sup> in YInO<sub>3</sub>-1175.

The observation of a higher asymmetric ratio in hexagonal YInO<sub>3</sub> has a very important structural implication as well. In a lucid review by Sleight *et al.*<sup>5</sup> it is described that YInO<sub>3</sub> occurs in two types of polymorphic hexagonal modifications. The one which shows a paraelectric behavior (space group: *P*<sub>6<sub>3</sub>*mmc*) actually has Y atoms at an inversion center, the O to Y polyhedra is a trigonal antiprism and two capped oxygens which are at equal distances and far off are in the first co-ordination sphere. However, in the functional ferroelectric form (space group: *P*<sub>6<sub>3</sub>*cm*), the capping Y–O distances alternate between long and short and the Y–O polyhedra is now an asymmetric capped trigonal antiprism.<sup>5</sup> Many a times, it is difficult to distinguish between the *P*<sub>6<sub>3</sub>*cm* and *P*<sub>6<sub>3</sub>*mmc* modifications by XRD because of very small differences in their XRD patterns. Considering, that it is this subtle change that brings about the ferroelectric behavior in this class of compounds, it would be really helpful if this distinction between the two polymorphs can also be revealed by a complementary technique. In the case of hexagonal YInO<sub>3</sub> (unlike the C-type polymorph), Y and In occupy distinct sites and by virtue of the ionic radius as well as the non-preference for a five co-ordinated site occupied by In<sup>3+</sup>, Eu<sup>3+</sup> is expected to occupy Y<sup>3+</sup>-sites. Assuming that majority of Eu<sup>3+</sup> lies in the Y<sup>3+</sup> site, a strong ED transition along with the observation of the <sup>5</sup>D<sub>0</sub>→<sup>7</sup>F<sub>0</sub> transition, suggests a highly asymmetric site for Y<sup>3+</sup> in YInO<sub>3</sub>. This emphasizes</sub></sub></sub></sub>

that hexagonal YInO<sub>3</sub> is obtained in the ferroelectric *P*<sub>6<sub>3</sub>*cm* structure.<sup>14</sup></sub>

### 3.5 Judd–Ofelt theory: validation of experimental results

The Judd–Ofelt theory has been successfully applied to the quantitative determination of the optical properties of trivalent lanthanides.<sup>22,23</sup> The Judd–Ofelt analysis of the emission spectrum is a powerful tool for calculating the parity-forbidden electric-dipole radiative transition rates between the various levels of a rare earth ion such as Eu<sup>3+</sup>. Through these analyses, the local environment around the metal ion and the bond covalency of M–L bonds can be interpreted. It is possible to determine the J–O intensity parameters  $\Omega_\lambda$  (where  $\lambda = 2, 4$  and  $6$  *etc.*) from the emission spectral data. Moreover, it is also possible to determine the radiative transition rate ( $A_R$ ), radiative lifetimes ( $\tau_R$ ) and the quantum efficiency for any given system from the emission spectrum.

Hence, in order to further substantiate the observation and gain deeper insight into the local environment around Eu<sup>3+</sup> in the nano and bulk C-type YInO<sub>3</sub> and hexagonal YInO<sub>3</sub>, the intensity parameters ( $\Omega_\lambda$ ) where  $\lambda = 2$  and  $4$  along with the radiative ( $A_{rad}$ ) and non-radiative ( $A_{nrad}$ ) rates for Eu<sup>3+</sup> ions in both the samples were determined from the emission spectra. The application of the JO theory to the quantitative analysis of Eu<sup>3+</sup> emissive properties in the matrix is nicely presented by Werts *et al.*<sup>24,25</sup>

The experimental intensity  $\Omega_\lambda$  can be calculated from the ratio of the intensity of the <sup>5</sup>D<sub>0</sub>→<sup>7</sup>F<sub>1</sub> ( $\lambda = 2, 4, 6$ ) transitions,  $\int I_1(\nu)d\nu$ , to the intensity of the <sup>5</sup>D<sub>0</sub>→<sup>7</sup>F<sub>1</sub> transition,  $\int I_1(\nu)d\nu$  as follows:

$$\Omega_\lambda = \frac{D_{MD}\nu_1^3}{e^2\nu_\lambda^3} \frac{9n^3}{n(n^2 + 2)^2 |\langle \psi J || U^{(\lambda)} || \psi' J' \rangle|^2} \frac{\int I_\lambda(\nu)d\nu}{\int I_1(\nu)d\nu} \quad (1)$$

The probabilities of each spontaneous emission (radiative rates) can be obtained from eqn (1) using calculated  $\Omega_\lambda$  parameters. The total radiative lifetime can be represented as the reciprocal of the total radiative decay rate, *i.e.*  $\tau_R = 1/A_R$ . From the experimental decay time ( $\tau_f$ ) and  $\tau_R$  values, the  $\tau_{NR}$  *i.e.* the non-radiative life times can be calculated.

In order to calculate J–O parameters using eqn (1) the average transition energies are obtained from the emission spectra as an average over the selected transition region:

$$\nu_\lambda = \frac{\int_\lambda \nu I(\nu)d\nu}{\int_\lambda I(\nu)d\nu} \quad (\lambda = 0, 1, 2, 3 \text{ and } 4)$$

Since the emission band for the <sup>5</sup>D<sub>0</sub>→<sup>7</sup>F<sub>6</sub> transition, centered at around 810 nm, could not be detected due to the limitation of the measurement spectral range, we can only determine the values of  $\Omega_2$  and  $\Omega_4$  parameters. However, it has been shown that the influence of  $\Omega_6$  can be neglected in the determination of radiative properties of Eu<sup>3+</sup> ions.<sup>26,27</sup> For the calculation we have adopted a value of 2.04 for the index of refraction which has been calculated from the refractive index values of its constituents employing the Gladstone Dale equation. Taking into account that the index of refraction is

wavelength dependent; taking the constant value into calculation introduces a small error in the obtained values since the refractive index changes are small over the wavelength region of interest (570–710 nm). This simplification is justified for the sake of comparison of JO parameters between the samples since this cannot change the observed trends. In general, the parameter  $\Omega_2$  is related to the covalency and structural changes in the vicinity of the  $\text{Eu}^{3+}$  ion (short range effect) and  $\Omega_4$  and  $\Omega_6$  are related to the long-range effects.

The J–O parameters, as determined for the  $\text{Eu}^{3+}$  ions  $\text{YInO}_3$ -600,  $\text{YInO}_3$ -900 and  $\text{YInO}_3$ -1175, are mentioned in Table 1. The J–O intensity parameters ( $\Omega_j$ ) of the  $\text{Eu}^{3+}$  ion in this matrix reveal information regarding the covalence and surrounding of the metal ion. These are significant because,  $\Omega_2$  is related to the covalency and structural changes in the vicinity of the  $\text{Eu}^{3+}$  ion (short range effect) and  $\Omega_4$  is related to the long-range effects. In general, the higher values of the above parameter indicate an increase in polarizability and an associated increase in the covalent character of the  $\text{Eu}^{3+}$  environment. The higher value of the ratio  $\Omega_2/\Omega_4$ , as observed for the nanoparticle  $\text{YInO}_3$ -600, indicates that the distortion around  $\text{Eu}^{3+}$  ions is more in the nano regime than in the bulk sample. Further, the greater individual values of  $\Omega_2$  and  $\Omega_4$  also indicate the greater extent of the covalent character/electron density around the  $\text{Eu}^{3+}$  ion in nanoparticles. The non-radiative decay rate is also found to be higher for nanoparticles thus pointing towards the appreciable amount of surface defects providing alternative pathways and leading to reduced emission and life times. On comparing the J–O parameters for the two polymorphs,  $\Omega_2$  is observed to be less than  $\Omega_4$  for  $\text{YInO}_3$ -1175 which ascertains the presence of  $\text{Eu}^{3+}$  in a highly asymmetric environment whereas reverse trends are observed in the case of  $\text{YInO}_3$ -900.

It is noteworthy that all these calculations support the experimental observation of optical properties like asymmetry ratios, luminescence intensities and lifetime values.

### 3.6 Potential application of various polymorphs as luminescent materials

Other than providing a structural basis for the luminescence behaviour of  $\text{Eu}^{3+}$  in the  $\text{YInO}_3$  lattice, the study brings forth a candidate for phosphor applications which have been hitherto unexplored. The relatively higher intensities of the red emission in the nano C-type  $\text{YInO}_3$  and in hexagonal  $\text{YInO}_3$  samples make them important candidates for red phosphors. This is significant in the context of the search for  $\text{Eu}^{3+}$ -based red phosphors with a greater purity of red emission. More importantly, the hexagonal polymorph which has the highest asymmetry ratio and shows the best luminescence properties among these three shows immense promise. It is further attractive because of the reasonably high fluorescence yield depicted by this system which can be attributed to lesser non-radiative pathways as is also supported by the calculated non-radiative decay constants. To evaluate the material performance on color luminescence emission, CIE chromaticity coordinates were evaluated for  $\text{YInO}_3$ -900 and  $\text{YInO}_3$ -1175 samples

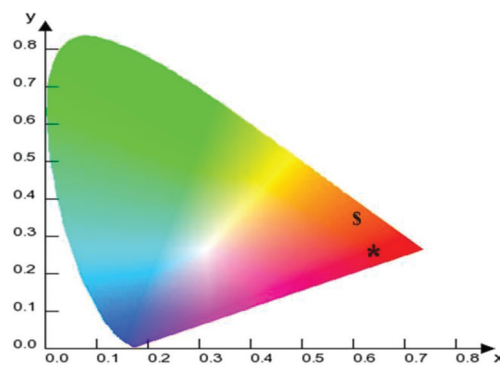


Fig. 7 CIE diagram showing the coordinates and representing the color emitted by  $\text{YInO}_3$ -900 (\$) and  $\text{YInO}_3$ -1175 (\*).

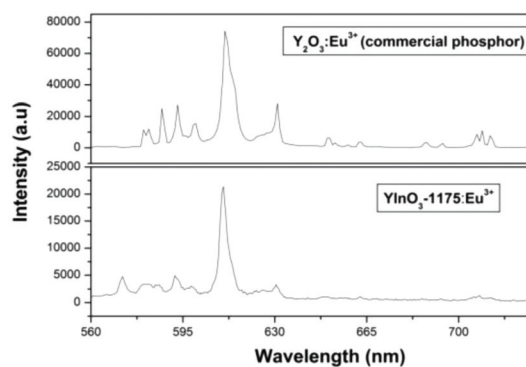


Fig. 8 Comparison of the PL data of the  $\text{Eu}^{3+}$  doped  $\text{YInO}_3$  sample with a commercial red phosphor.

adopting standard procedures. It is clear from the values that  $\text{YInO}_3$ -900 gives an 'orangish-red' emission due to the presence of relatively intense 592 nm lines ( $^5\text{D}_0 \rightarrow ^7\text{F}_1$ ). The color can be tuned to pure red when annealed at 1175 °C. This is represented as the point '\*' in the CIE diagram shown in Fig. 7.

To get an idea about the luminescence efficiency and commercial utility of the gel-combustion derived yttrium indate sample, its PL intensity was compared with that of a commercial red phosphor sample ( $\text{Y}_2\text{O}_3:\text{Eu}$ , NP-340, Nichia, Japan) under identical conditions. For this, the entire emission spectrum was integrated and the value was compared with that of the commercial phosphor samples (Fig. 8). It was observed that the PL intensity of the hexagonal  $\text{YInO}_3$  was 35% of the commercial sample.

## 4. Conclusions

In summary, this study explores a single compound,  $\text{YInO}_3$  for the size and polymorph induced tunability of its luminescence behavior by employing  $\text{Eu}^{3+}$  as a structure-sensitive luminescent probe. The metastable C-type  $\text{YInO}_3$  could be obtained by

a non-equilibrium gel combustion synthesis which on controlled annealing yielded a hexagonal polymorph at 1175 °C. After extensive characterization by X-ray diffraction and Raman spectroscopy, the luminescence behavior of the bulk and nano C-type YInO<sub>3</sub> were compared and were further analysed with respect to the local site symmetry in hexagonal YInO<sub>3</sub>. The high asymmetry ratio and lesser lifetime of nano C-type as compared to the bulk C-type YInO<sub>3</sub> was attributed to higher asymmetry and the non-radiative decays in nanoparticles due to the higher surface content of Eu<sup>3+</sup>. A marked increase in the asymmetry ratio coupled with higher lifetime in the hexagonal polymorph confirmed the existence of a ferroelectric *P*<sub>6<sub>3</sub>cm modification for hexagonal YInO<sub>3</sub>. The J–O parameters were determined which were in confirmation with experimental results. Low phonon energy and high purity of red emission coupled with good fluorescence quantum yields highlight the potential of a hitherto unexplored hexagonal YInO<sub>3</sub> as a promising phosphor.</sub>

## Notes and references

- N. S. Karan, S. Sarkar, D. D. Sarma, P. Kundu, N. Ravishankar and N. Pradhan, *J. Am. Chem. Soc.*, 2011, **133**, 1666.
- C. J. Jia, L. D. Sun, Z. G. Yan, Y. C. Pang, S. Z. Lu and C. H. Yan, *Eur. J. Inorg. Chem.*, 2010, 2626.
- M. Zhao, G. Li, J. Zheng, L. Li, H. Wang and L. Yang, *CrystEngComm*, 2011, **13**, 6251.
- D. M. Giaquinta and H.-C. zur Loye, *Chem. Mater.*, 1994, **6**, 365.
- A. W. Sleight, *Prog. Solid State Chem.*, 2009, **37**, 251.
- C. W. F. T. Pistorius and G. J. Kruger, *J. Inorg. Nucl. Chem.*, 1976, **38**, 1471.
- J. Ding, J. Bao, S. Sun, Z. Luo and C. Gao, *Dyes Pigm.*, 2011, **91**, 501.
- J. Ding, W. Yan, W. Xie, S. Sun, J. Bao and C. Gao, *Nano-scale*, 2014, **6**, 2299.
- T. Tohei, H. Moriwake, H. Murata, A. Kuwabara, R. Hashimoto, T. Yamamoto and I. Tanaka, *Phy. Rev. B: Condens. Matter*, 2009, **79**, 144125.
- B. B. Van Aken, T. T. M. Palstra, A. Filippetti and N. A. Spaldin, *Nat. Mater.*, 2004, **3**, 164.
- V. Grover, R. Shukla, D. Jain, S. K. Deshpande, A. Arya, C. G. S. Pillai and A. K. Tyagi, *Chem. Mater.*, 2012, **24**, 2186.
- WinPLOT, J. Rodríguez-Carvajal, Laboratoire Leon Brillouin (CEA-CNRS), April 2005 (LLB-LCSIM).
- V. Grover, S. N. Achary and A. K. Tyagi, *J. Appl. Crystallogr.*, 2003, **36**, 1082.
- R. Shukla, V. Grover, S. K. Deshpande, D. Jain and A. K. Tyagi, *Inorg. Chem.*, 2013, **52**, 13179.
- R. Shukla, F. N. Sayed, V. Grover, S. K. Deshpande, A. Guleria and A. K. Tyagi, *Inorg. Chem.*, 2014, **53**, 10101.
- H. Zhang, Q. Yang, B. Zhang and S. Lu, *J. Raman Spectrosc.*, 2011, **42**, 1384.
- W. H. Weber, K. C. Hass and J. R. McBride, *Phys. Rev. B: Condens. Matter*, 1993, **48**, 178.
- M. N. Iliev, H. G. Lee, V. N. Popov, M. V. Abrashev, A. Hamed, R. L. Meng and C. W. Chu, *Phys. Rev. B: Condens. Matter*, 1997, **56**, 2488.
- S. K. Gupta, M. Sahu, K. Krishnan, M. Saxena, V. Natarajan and S. V. Godbole, *J. Mater. Chem. C*, 2013, **1**, 7054.
- S. K. Gupta, P. S. Ghosh, N. Pathak, A. Arya and V. Natarajan, *RSC Adv.*, 2014, **4**, 29202.
- X. Y. Chen and G. K. J. Liu, *J. Solid State Chem.*, 2005, **178**, 419.
- G. S. Ofelt, *J. Chem. Phys.*, 1962, **37**, 511.
- B. R. Judd, *Phys. Rev.*, 1962, **127**, 750.
- M. H. V. Werts, R. T. F. Jukes and J. W. Verhoeven, *Phys. Chem. Chem. Phys.*, 2002, **4**, 1542.
- W. T. Carnall, P. R. Fields and K. Rajnak, *J. Chem. Phys.*, 1968, **49**, 4424.
- R. Balakrishnaiah, R. Vijaya, P. Babu, C. K. Jayasankar and M. L. P. Reddy, *J. Non-Cryst. Solids*, 2007, **353**, 1397.
- K. Marimuthu, R. T. Karunakaran, S. Surendra Babu, G. Muralidharan, S. Arumugam and C. K. Jayasankar, *Solid State Sci.*, 2009, **11**, 1297.